JGR Space Physics

TECHNICAL REPORTS: METHODS

10.1029/2021JA029511

Measurements of the Net Charge Density of Space Plasmas

Chao Shen[1], Yufei Zhou[1], Lai Gao[1], Xiaogang Wang[2], Zuyin Pu[3], C. Philippe Escoubet[4], and J. L. Burch[5]

[1]School of Science, Harbin Institute of Technology, Shenzhen, China, [2]School of Physics, Harbin Institute of Technology, Harbin, China, [3]School of Earth and Space Sciences, Peking University, Beijing, China, [4]ESA/ESTEC (SCI-SC), Noordwijk, The Netherlands, [5]Southwest Research Institute, San Antonio, TX, USA

Key Points:

- Charge densities in geomagnetopause have been calculated using MMS electric field measurements
- A method for extracting the charge density from 10-point electric potential measurements is presented
- An additional scheme to measure the charge density using seven or eight electric potential probes is explored

Supporting Information:

Supporting Information may be found in the online version of this article.

Correspondence to:

C. Shen,
shenchao@hit.edu.cn

Citation:

Shen, C., Zhou, Y., Gao, L., Wang, X., Pu, Z., Escoubet, C. P., & Burch, J. L. (2021). Measurements of the net charge density of space plasmas. *Journal of Geophysical Research: Space Physics*, *126*, e2021JA029511. https://doi.org/10.1029/2021JA029511

Received 30 APR 2021
Accepted 12 NOV 2021

Author Contributions:

Conceptualization: Chao Shen
Data curation: Yufei Zhou, Lai Gao, J. L. Burch
Formal analysis: Chao Shen
Funding acquisition: Chao Shen
Investigation: Chao Shen
Methodology: Chao Shen
Project Administration: Chao Shen
Resources: Chao Shen
Software: Yufei Zhou, Lai Gao
Supervision: Chao Shen
Validation: Yufei Zhou, Lai Gao, Xiaogang Wang, Zuyin Pu, C. Philippe Escoubet, J. L. Burch
Visualization: Yufei Zhou, Lai Gao

Abstract Space plasmas are composed of charged particles that play a key role in electromagnetic dynamics. However, to date, there has been no direct measurement of the distribution of such charges in space. In this study, three schemes for measuring charge densities in space are presented. The first scheme is based on electric field measurements by multiple spacecraft. This method is applied to deduce the charge density distribution within Earth's magnetopause boundary layer using Magnetospheric MultiScale constellation (MMS) four-point measurements, and indicates the existence of a charge separation there. The second and third schemes proposed are both based on electric potential measurements from multiple electric probes. The second scheme, which requires 10 or more electric potential probes, can yield the net charge density to first-order accuracy, while the third scheme, which makes use of seven to eight specifically distributed probes, can give the net charge density with second-order accuracy. The feasibility, reliability, and accuracy of these three schemes are successfully verified for a charged-ball model. These charge density measurement schemes could potentially be applied in both space exploration and ground-based laboratory experiments.

1. Introduction

Electromagnetic fields are omnipresent in space. They control the motion of plasmas, and the transportation, release, and transformation of energy in space, and thereby are the key driver of space weather hazards. Charges and electric currents (flows of charged particles) source the electromagnetic field, and therefore the distribution and motions of charges determine its form. Charge separations occur in electric double layers, which exist commonly in space plasmas (Akasofu, 1981; Block, 1975; Raadu, 1989). Net charges can appear in plasma boundary layers (Parks, 1991), for example, the magnetopause boundary layers and Alfvén layers (Hasegawa & Sato, 1989). Charge separations can also occur during ambipolar diffusion processes (Alfvén & Falthammar, 1963; Bittencourt, 2004), for example, the Earth's polar wind (Axford, 1968; Lemaire & Pierrard, 2001; Yau et al., 2007). In macro-scale plasmas, flow shears or vorticities can accumulate these net charges, driving the field-aligned currents (Michael, 2014). Charge separations also play a key role in plasma instabilities, for example, the Rayleigh-Taylor instability (Michael, 2014; Treumann & Baumjohann, 1997) and the tearing instability (Treumann & Baumjohann, 1997).

The charge separations in space plasmas can appear at various spatial scales. The plasmas with no magnetic field are commonly electrically neutral when the spatial scale is much larger than the Debye length and the temporal scale is rather longer than the plasma oscillation time (Bittencourt, 2004). At the Debye length space scale or plasma oscillation time scale, the electrical neutrality would be violated and charge separations appear. On the other hand, the ambipolar diffusion takes place in inhomogeneous plasmas due to the different thermal velocities of the electrons and ions, and polarization electric fields will be created, which can span several Earth radii in the Earth's polar wind regions (Axford, 1968; Lemaire & Pierrard, 2001). However, due to the difference between the parameters of electrons and ions, the charge separations in magnetized plasmas at spatial scales much larger than the Debye length can occur. As for the magnetopause boundary layers, the protons of solar wind can penetrate more deeply into the magnetosphere than electrons because of their greater gyroradius. Therefore, the magnetosphere and magnetosheath sides of the magnetopause boundary layer are positively and negatively charged, respectively, and the width of the magnetopause boundary layer is at the order of proton gyroradius (several hundred kilometers) (Hughes, 1995; Parks, 1991). During the magnetospheric substorms, the plasmas are injected from the magnetotail into the inner magnetosphere, and the ions and electrons are energized and drift duskward and dawnward, respectively. As a result, the duskside and dawnside of the inner magnetosphere accumulate

Writing – original draft: Chao Shen, Yufei Zhou
Writing – review & editing: Chao Shen

positive and negative charges, respectively, and a dawnward shielding electric field with a spatial scale of several Earth radius is established (Hasegawa & Sato, 1989).

The acquisition of a spatial distribution of electric charge density is of critical importance for recognizing and understanding the dynamics of electromagnetic fields and plasmas in space. However, there is still no equipment available for directly measuring the net charge density in space, although measurements of the charge density in the atmosphere near the ground have been achieved. The difficulty of such measurements in space arises because the plasmas there are extremely thin, with only a few charged particles per cm^3, and the net charge density is even lower by several orders. According to Harris (1962), the maximum charge density within the magnetopause boundary layer is $|\rho|_{\max} \approx 2ne(1 - V^2/c^2)^{-2}V^2/c^2$, where n is the number density of the plasmas, V is the drifting velocity of electrons and ions, c is the free speed of light in vacuum. According to Lee and Kan (1979), the main carriers of the current in the magnetopause are ions, whose temperature is about 300 eV and thermal velocity is estimated to be $V \approx 200\ km/s$. Assume $n \approx 10\ cm^{-3}$ in the magnetopause, then $|\rho|_{\max} \approx 10\ e/m^3$.

Cluster mission has first achieved the four-point measurements on the electric field in space (Escoubet et al., 2001), with which the electric field structure of the magnetopause boundary layer has been revealed (Haaland et al., 2021; Paschmann et al., 2005; and references therein). The Magnetospheric MultiScale (MMS) constellation (Burch et al., 2016) can measure the three-dimensional electric field vector at four locations in space so as to obtain the linear gradient of the electric field. By using this advantage, Tong et al. (2018) have deduced the spatial distribution of net charge within a magnetic hole and found there are net positive charges in the center of the magnetic hole and an electron sheath around the hole. With a similar approach, Argall et al. (2019) have investigated the distribution of charge density in the diffusion region of magnetic reconnection. However, we still have no independent charge density measurement equipment in space. In this article, we will explore how the charge density can be deduced based on multiple-probe electric potential measurements onboard a single spacecraft.

In Section 2, we first discuss the method for deducing the charge density from four-point electric field measurements, which has been applied to analyze the charge density distribution in the dayside magnetopause boundary layer during an MMS magnetopause crossing event. In Section 3, a method for deducing the charge density from ≥10-point electric potential measurements is studied. Section 4 explores measurements of the charge density based on seven or eight electric potential probes. Section 5 gives a summary and some discussion.

2. Deducing the Charge Density From Multi-Spacecraft Electric Field Measurements

The direct approach to obtain the net charge density is to sum up the charge densities of positively and negatively charged particles with the formula

$$\rho = -e\, n_e + \sum_i \ q_i \ n_i, \tag{1}$$

where n_e and n_i are the densities of the electrons and the ith ion, respectively, and q_i is the charge of the ith ion. However, the electric force is so strong that the plasmas are always quasi-neutral, and the separation between the two types of charges is very slight. Therefore, the charge densities in space plasmas are extremely small. It is almost impossible to determine the net charge density by measuring the densities of charged particles at the present stage of space exploration.

The most feasible and practicable method at present is to deduce the net charge density by measuring the electric potentials or electric fields created by the net charges at high accuracies with well-developed technology (Michael, 2014; Mozer & Bruston, 1967; Mozer, 1973; Paschmann et al., 1997; Pedersen et al., 1998). The Spin-plane Double Probes (SDPs) and Axial Double Probes (ADPs) (Torbert et al., 2016; Lindqvist et al., 2016; Ergun et al., 2016) onboard the four spacecraft of the MMS constellation (Burch et al., 2016) yield four electric field vectors at four different locations separated by tens of kilometers. With the Gaussian theorem, $\rho = \varepsilon_0 \nabla \cdot \mathbf{E}$, we can get the charge density at the center of the constellation, as illustrated in Figure 1. Suppose that the four spacecrafts of the MMS constellation are located at four different positions $\mathbf{r}_\alpha$ $(\alpha = 1, 2, \cdots, 4)$. The barycenter of the MMS constellation is $\mathbf{r}_c \equiv \frac{1}{4}\sum_{\alpha=1}^{4} \mathbf{r}_\alpha$. It is convenient to assume that $\mathbf{r}_c = 0$, so that the barycenter of the constellation is the origin of the frame of reference. The four spacecraft yield four electric fields,

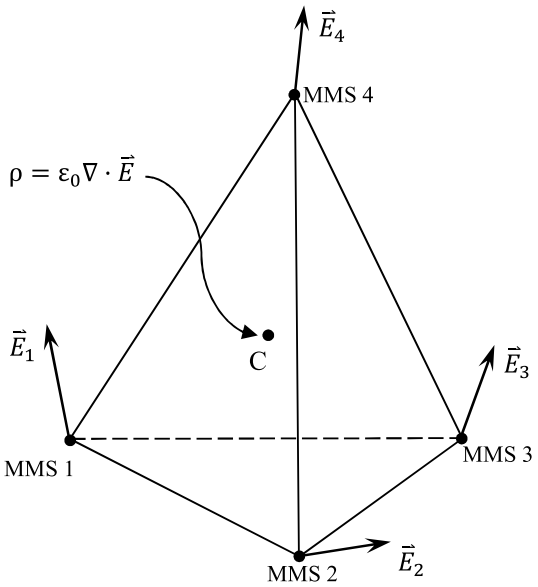

Figure 1. A schematic view of the measurements of the electric field by the MMS constellation and the calculation of the charge density.

$\mathbf{E}_\alpha = \mathbf{E}(\mathbf{r}_\alpha)$, $\alpha = 1, 2, \cdots, 4$. Under the linear assumption, the ith component of the gradient of the electric field at the barycenter can be calculated as (Chanteur, 1998; Harvey, 1998)

$$(\nabla_i \mathbf{E})_c = \frac{1}{4} \sum_{\alpha=1}^{4} \mathbf{E}_\alpha r_{\alpha j} R_{ji}^{-1}, \tag{2}$$

where $R_{ij} = \frac{1}{4} \sum_{\alpha=1}^{4} r_{\alpha i} r_{\alpha j}$ is the volumetric tensor of the constellation (Harvey, 1998), and R_{ji}^{-1} its inverse. By using the Gaussian theorem, we can get the charge density with the divergence of the electric field vector, that is,

$$\rho = \varepsilon_0 \nabla \cdot \mathbf{E} = \varepsilon_0 \sum_{i=1}^{3} \nabla_i E_i, \tag{3}$$

The accuracy of the axial electric field measured by MMS is 1 mV/m (ADPs, Ergun et al., 2016), while the accuracy of the components of electric field in the spin plane is <0.5 mV/m (SDPs, Lindqvist et al., 2016). The two corresponding errors can be denoted as $\delta E_A \sim 1$ mV/m and $\delta E_S \sim 0.5$ mV/m, respectively. It is known that the characteristic spatial scale of MMS is $L \approx 20$ km. Therefore, the error of the charge density calculated from the MMS four-point electric measurements is estimated to be $\delta\rho \approx \varepsilon_0(\frac{\delta E_A}{L} + 2\frac{\delta E_S}{L}) \approx 0.45$ e/m^3 which, as we will see in a case study, is much smaller than the observed charge density. The algorithm presented here is also evaluated and validated by a more sophisticated simulation shown in Figures S1 and S2.

Here we will explore the net charge distribution within the magnetopause boundary layer based on MMS electric measurements. It is well known that a charge separation occurs in the magnetopause, brought about by the effects of inertia (because there is a large difference between the masses of the electrons and ions). As a result of that, the net positive charges accumulate at the magnetospheric side and the net negative charges accumulate at the magnetosheath side of the magnetopause boundary. Because the MMS constellation has a rather small size (with the spacecraft separations being several tens of kilometers) and can be well-embedded in the magnetopause boundary, the charge density can be deduced from the MMS electric observations using the above method. We investigated one MMS magnetopause crossing event at 14:26:14 on November 11, 2015 by examining the electric field and calculating the charge density, whose values during the crossing event are shown in Figure 2. It can be seen that the rotational discontinuity (RD) appear at UT14:26:40 with the maximum magnetic rotation rates (panel (d)) (C. Shen et al., 2007), minimum value of the gradient of the magnetic strength (panel (e)), and smallest radius of curvature of the magnetic field lines (panel (f)). As shown in panel (g), a charge separation is evident within the magnetopause boundary, with the positive charges at the magnetospheric side and negative charges at the magnetosheath side. The maximum value of the charge density in the magnetopause is about 60e/m^3, which is much larger than the error ($\delta\rho \approx 0.45$ e/m^3) as given above. It is evident that the electric neutrality is kept in the magnetosheath near to the magnetopause. These results are in agreement with the conventional kinetic models of the magnetopause boundary layers (Harris, 1962; Hughes, 1995; Lee & Kan, 1979; Parks, 1991).

3. Charge Density Measurements From 10 Probes on Board a Spacecraft-Stiff Booms Method

It is known that the linear gradient of a quantity can be estimated based on four-point measurements (Chanteur, 1998; Harvey, 1998; C. Shen et al., 2003), while the quadratic gradient of a quantity can be calculated based on 10-point measurements (Chanteur, 1998). In the low Earth Orbit missions DEMETER (Berthelier et al., 2005) and Zhangheng-1 (X. H. Shen et al., 2018), the electric field is measured with four probes mounted at the ends of four stiff booms. We suggest to construct an electric equipment composed of 10 or more electric probes so that both the electric field and charge density can be measured. In a previous investigation (C. Shen

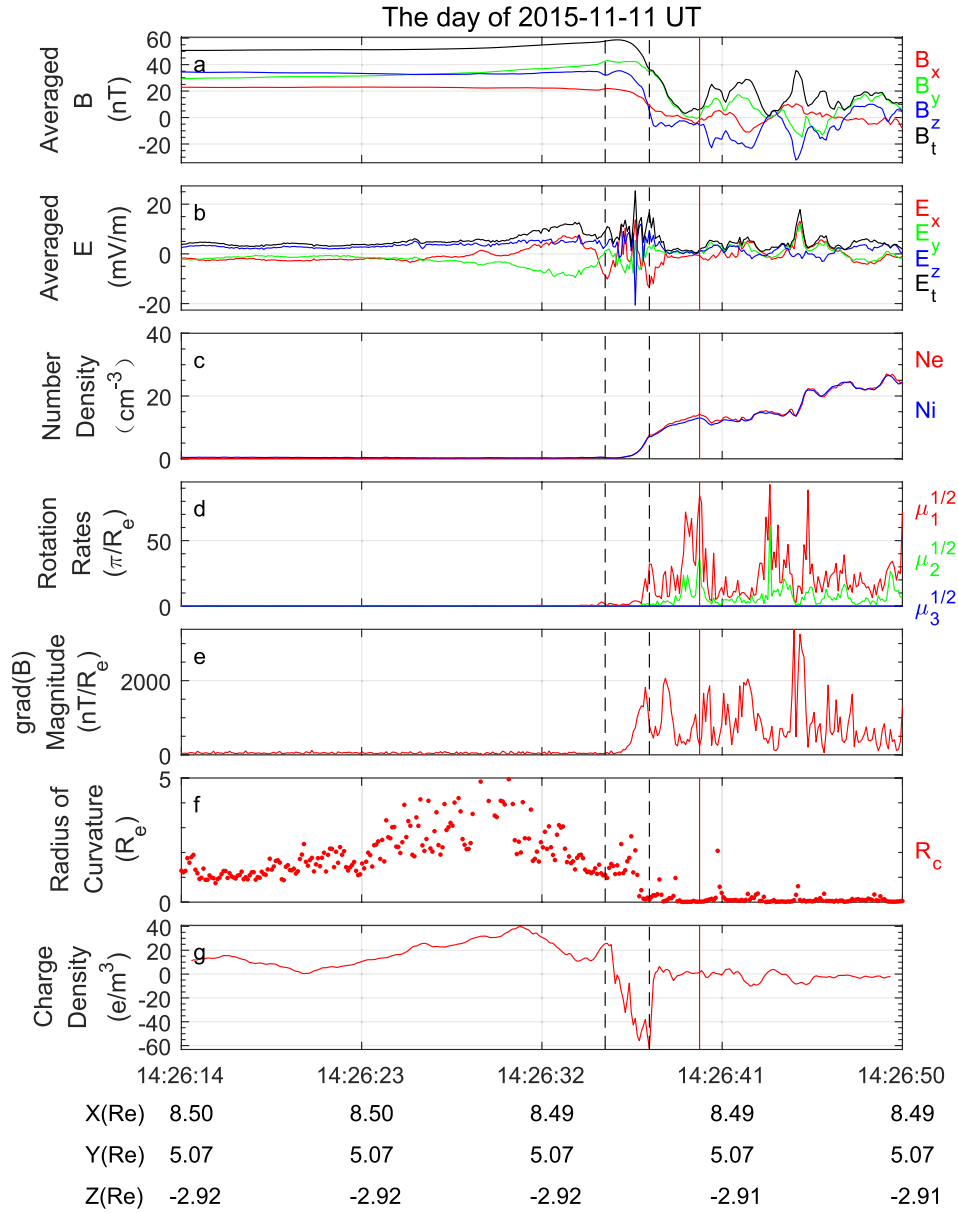

Figure 2. The structure of the magnetopause during an MMS crossing event on November 11, 2015. From top to bottom: (a) the magnetic flux density at the center of the constellation, (b) the electric field at the center of the constellation, (c) the electron and ion number densities measured by MMS-1 (Pollock et al., 2016), (d) the rotation rates of the magnetic field (C. Shen et al., 2007), (e) $|\nabla|\boldsymbol{B}||$, (f) the radius of curvature of the magnetic field lines (C. Shen et al., 2003), and (g) the charge distribution. The red vertical line marks the largest rotation rates, and the black vertical dotted lines mark the largest and the smallest charge densities.

et al., 2021), a new algorithm was put forward to calculate the linear and quadratic gradients jointly based on 10 or more measurements. It can be applied to obtain the quadratic gradients ($\nabla^2\varphi$) from 10-point electric potential field (φ) measurements. Moreover, with the Poisson equation,

$$\rho = -\varepsilon_0\nabla^2\varphi, \tag{4}$$

it yields the distribution of the electric charge density. For the processes with temporal variations, the general governing equation is the d'Alembert equation, $-c^{-2}\partial_t^2\varphi + \nabla^2\varphi = -\varepsilon_0{}^{-1}\rho$, instead. However, for slow varying structures or steady structures and low-frequency plasma waves with their motion speeds much less than c, the first term at the right-hand side of the d'Alembert equation can be neglected.

Table 1
The Locations of the 10 Probes in the Barycenter Coordinates

x	y	z
−0.16474	0.520923	−0.07516
−0.29774	−0.2433	−0.00151
0.107263	−0.00029	0.243785
−0.12458	−0.14707	0.116693
−0.11324	0.080113	−0.22108
0.505285	−0.29726	−0.0293
0.055479	0.300437	−0.28976
0.461577	−0.14647	−0.13865
−0.2916	0.323618	0.339179
−0.13771	−0.3907	0.055801

We can check the feasibility of this 10-probe scheme. The electric field generated by a uniformly charged ball will be used to test this approach. Supposing that the radius of the ball is r_0 and its charge density is ρ, we get the electric potential field analytically as,

$$\varphi(\mathbf{r}) = \begin{cases} -\frac{1}{6}\epsilon^{-1}\rho r^2 + \frac{1}{2\epsilon}r_0^2\rho & if \ \ r \ \leq \ r_0, \\ -\frac{1}{4\pi\epsilon}\frac{Q}{r} & if \ \ r \ > \ r_0, \end{cases} \tag{5}$$

where $Q = \frac{4}{3}\pi {r_0}^3 \rho$ is the total charge and r is the distance from the center of the ball to the measurement point. In the following modeling, constant values of 1 are assigned to ρ, r_0, and ϵ, that is, $\rho = r_0 = \epsilon = 1$. The positions of the 10 probes in the barycenter coordinates are generated randomly and presented in Tab. 1 and Figure 3. The three characteristic lengths of the distribution of the 10 probes (Harvey, 1998; Robert et al., 1998) are $a = 0.10, b = 0.06$, and $c = 0.03$. The reconstructed characteristic matrix $\mathfrak{R}^{MN}$ is

$$(\mathfrak{R}^{MN}) = \begin{pmatrix} 12.73 & -11.09 & -5.05 & 5.22 & 2.74 & 1.61 \\ -11.09 & 20.90 & 5.47 & -6.71 & -4.97 & -2.28 \\ -5.05 & 5.47 & 6.44 & -2.49 & -4.56 & -2.27 \\ 5.22 & -6.71 & -2.49 & 12.83 & -1.91 & 2.27 \\ 2.74 & -4.97 & -4.56 & -1.91 & 9.09 & 0.86 \\ 1.61 & -2.28 & -2.27 & 2.27 & 0.86 & 2.68 \end{pmatrix} 10^{-3}, \tag{6}$$

and its eigenvalues are given in Table 2.

We first investigate the behavior of the resultants with the number of iterations. D is the local characteristic scale of the electric field structure and is set equal to r in this model. It is assumed that the barycenter of the constellation is at $[0.1, 0, 0]$, and the probe separations L are reduced proportionally so that the relative measurement scale $L/D = 0.026$. The relative truncation error, $X_{algorithm}/X_{real} - 1$, is shown in Figure 4. With increasing numbers of iterations, the errors decrease and finally converge to certain fixed values. In this calculation, the solution

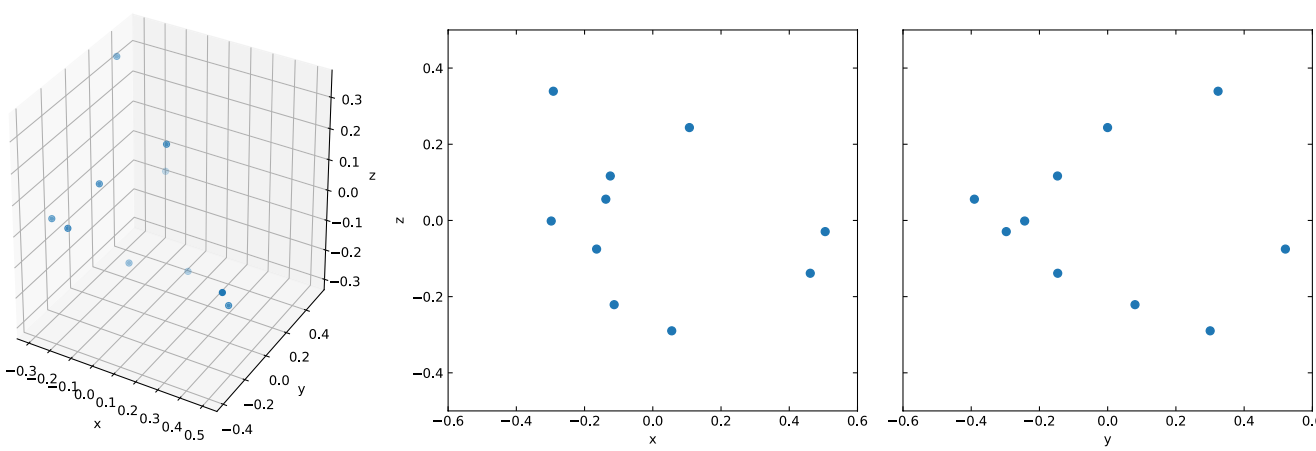

Figure 3. The distribution of the 10 probes.

Table 2
The Eigenvalues of the Characteristic Matrix $\mathfrak{R}^{MN}$

0.03614	0.01326	0.00114	0.00235	0.00510	0.00668

converges after 100 iterations. By testing various fields, we found that the number of iterations required for convergence varies.

Secondly, we investigate the dependence of the truncation errors on the relative measurement scale L/D. We have tested six situations, with the barycenter of the 10 probes located at three representative points within the ball, $[0.1, 0, 0]$, $[0.4, 0, 0]$, and $[0.7, 0, 0]$, and three points outside the ball, $[3, 0, 0]$, $[5, 0, 0]$, and $[8, 0, 0]$. We scale up and down the size of the original 10 probes to adjust the characteristic size L and therefore L/D.

Figure 5 shows the errors modeled in the ball. In general, the errors are less than $10^{-5}\%$ for the linear gradients and less than 0.02% for the quadratic gradients. With the same number of iterations, 1,000, the errors at different positions vary by order of 2. The extremely accurate results arise from the fact that the charge density has been assumed homogeneous and electric field is linear varying within the charged ball.

Figure 6 shows the modeling results outside of the ball. As $L/D < 0.01$, the relative errors of the non-vanishing quadratic gradient components are below 2%. The attained linear and quadratic gradients are accurate to second order and first order, respectively.

The same error analysis procedure for the 10-probe scheme has been applied to another charged ball model in which the charge density is inversely proportional to the square of the distance from the ball center, as shown in Figures S3 and S4, and a similar conclusion has been reached.

We further investigate the relationship between the accuracy of the density estimated and the number of probes used. Figure 7 indicates that the accuracy of the charge density is not improved significantly as the number of probes is increased. Therefore, 10 probes with a proper spatial configuration will be sufficient for robust measurements of the charge density.

This scheme is possible to be used for the net charge measurements on the low Earth orbits at the altitudes of several hundred kms, for which the 10 probes are mounted at the ends of 10 booms with different lengths, and the spacecraft can be either spinning or not.

The feasibility of the measurements at the low attitude Earth orbits can be shown by including observational errors. The accuracy of the probes is assumed at $\delta\phi \approx L\delta\nabla\phi \sim 10\ \text{m} \times \frac{0.5\,\text{mV}}{\text{m}} \sim 5\ \text{mV}$. The electric potential at an arbitrary probe can be expanded as the following.

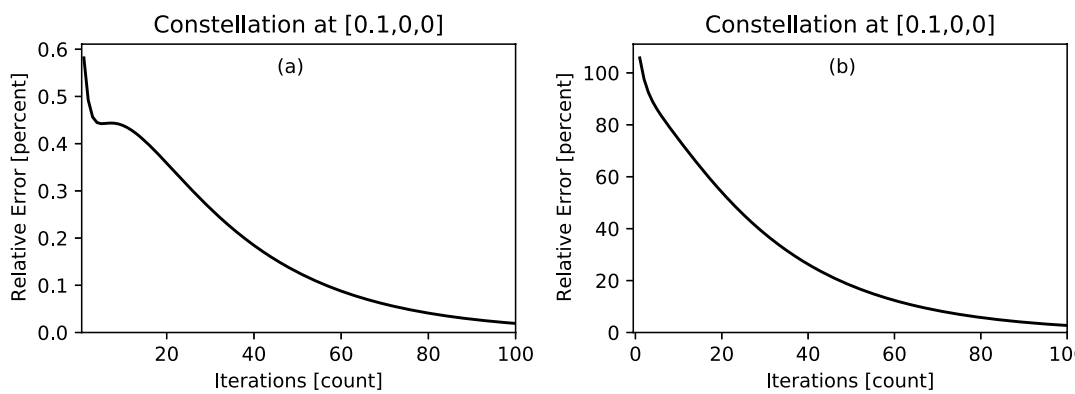

Figure 4. The relative errors of the linear (a) and the quadratic (b) electric potential gradients, that is, $\partial_x\phi$ and $\partial_x\partial_x\phi$, calculated for different numbers of iterations at $[0.1, 0, 0]$ within the uniformly charged ball.

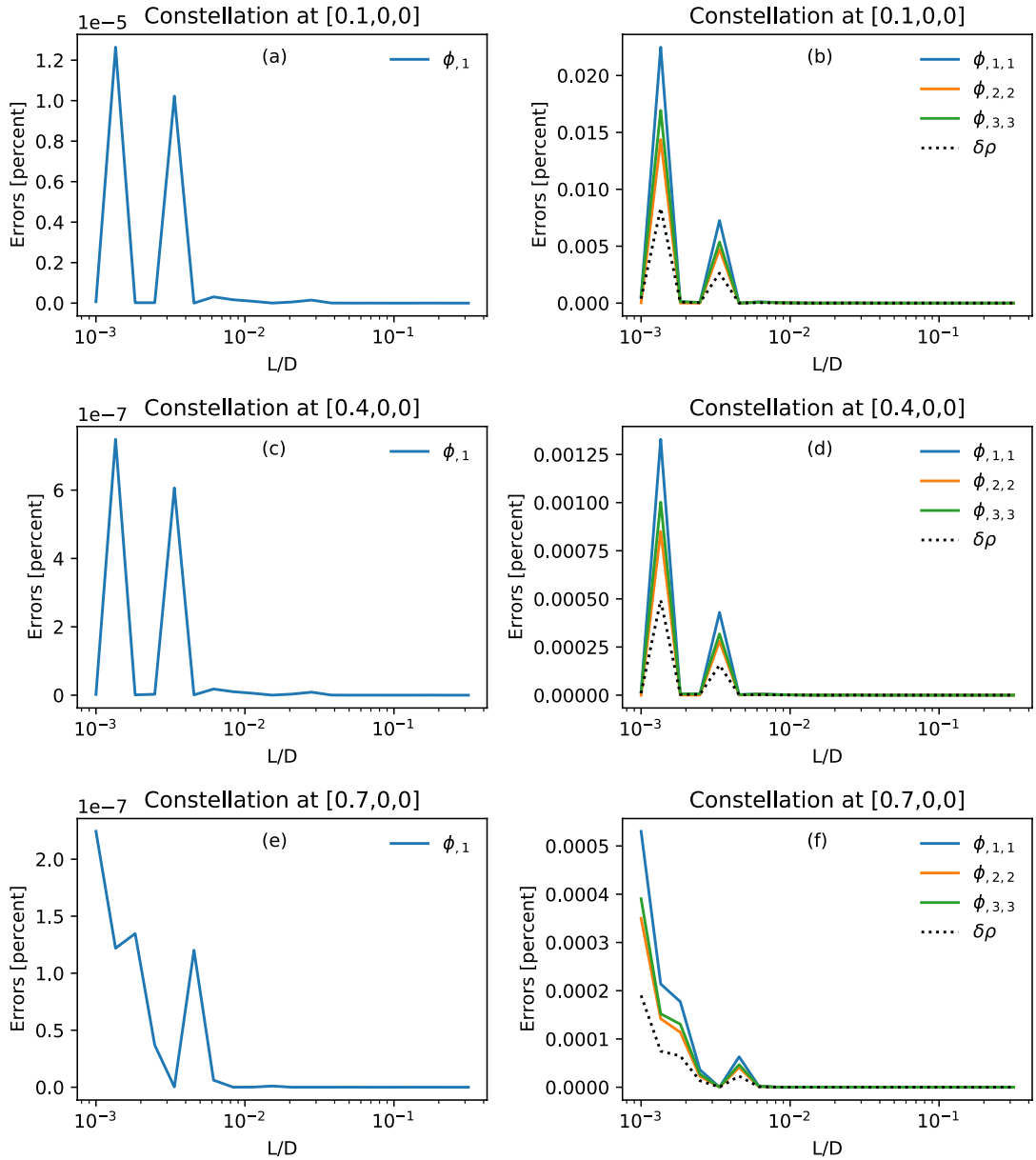

Figure 5. The variation of the errors of the calculation by using the 10-probe scheme with the relative measurement scale L/D for the case of a uniformly charged ball. The measurements are performed inside of the charged ball. The left panels, (a), (c), and (e), show the truncation errors for the non-vanishing component of the linear gradient by L/D calculated for three different locations of the barycenter of the 10 probes inside the ball, $[0.1, 0, 0]$, $[0.4, 0, 0]$, and $[0.7, 0, 0]$. The right panels, (b), (d), and (f), illustrate the relative errors of the non-vanishing components of the quadratic gradient and charge density (dashed line) calculated for the same three locations of the barycenter. It is noted that $\phi_{,1} \equiv \partial_x \phi$ and $\phi_{,2,2} \equiv \partial_y \partial_y \phi$, where a comma denotes partial differentiation.

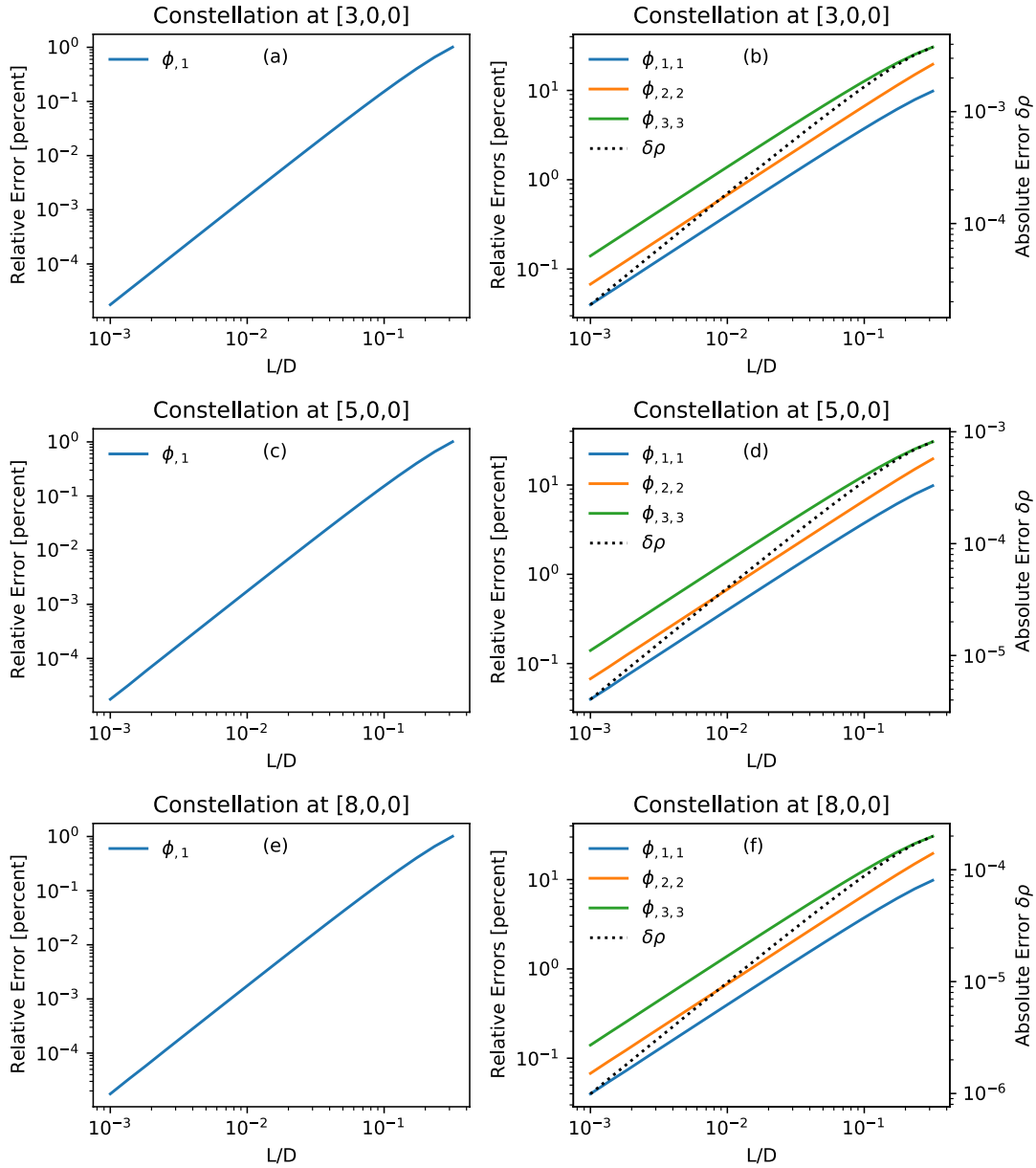

Figure 6. The dependence of the truncation errors of the calculations by using the 10-probe scheme on the relative measurement scale *L/D* for the case of a uniformly charged ball. The measurements are performed outside of the charged ball. The left panels, (a), (c), and (e), show the truncation error for the non-vanishing component of the linear gradient as a function of L/D calculated for three different locations of the barycenter of the 10 probes outside of the ball, $[3, 0, 0]$, $[5, 0, 0]$, and $[8, 0, 0]$. The right panels, (b), (d), and (f), illustrate the relative errors of the non-vanishing components of the quadratic gradient and the absolute value of the charge density (dashed line) calculated for the same three locations of the barycenter. It is noted that the real charge density outside of the ball is zero.

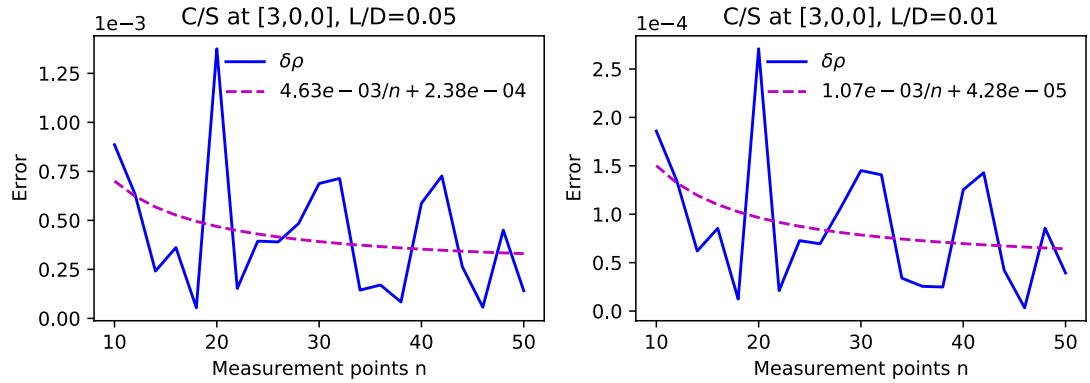

Figure 7. The relation between the absolute error of the charge density and the number of measurement points at [3, 0, 0]. The relative measurement scale is chosen as $L/D = 0.05$ (left) and $L/D = 0.01$ (right). The dashed lines are fitted from the modeled errors.

$$\begin{aligned}\phi &= \phi_c + \Delta\mathbf{x}\cdot\nabla\phi + \frac{1}{2}\Delta\mathbf{x}\ \ \Delta\mathbf{x}\cdot\nabla\nabla\phi \\ &\sim \phi_c - E\cdot L + \frac{1}{2}\frac{1}{\varepsilon_0}\rho\ \ L^2,\end{aligned} \tag{7}$$

where $\Delta\mathbf{x}$ is the distance of the probe from the center, which is at the scale of L; $\nabla\phi = -\mathbf{E}$, and $\nabla\nabla\phi$ is estimated by $\nabla^2\varphi = -\rho/\varepsilon_0$. The second term at the right-hand side (or the first-order term) is the contribution of the electric field, which is about $EL \sim 600\frac{\mathrm{mV}}{\mathrm{m}} \times 10\ \mathrm{m} \sim 6.0\ \mathrm{V}$. The third term (or the second-order term) is the contribution of the charge density, which is about $\frac{1}{2}\frac{1}{\varepsilon_0}\rho\ \ L^2 \sim 50\ \mathrm{mV}$ if the typical value of the charge density at low Earth orbits is assumed to be $\rho \sim 5\times 10^4 e/m^3$, which is about three order higher than those at the high Earth orbits. They are both much larger than the probe sensitivity ($5mV$), so that at low Earth orbits the charge density is observable with the approach described above.

4. Measuring the Charge Density With Seven or Eight Electric Potential Probes

Only three diagonal components of the quadratic gradient of the electric potential are contained in the Poisson equation ($\rho \propto \nabla^2\phi = \frac{\partial^2}{\partial x^2}\phi + \frac{\partial^2}{\partial y^2}\phi + \frac{\partial^2}{\partial z^2}\phi$). The three other cross-components of the quadratic gradient, $\partial_x\partial_y\phi$, $\partial_y\partial_z\phi$, and $\partial_z\partial_x\phi$, are of no use for computing the charge density, so three independent parameters can be neglected in this algorithm. Therefore, $10-3\ =\ 7$ probes are sufficient to acquire the data for the estimation of the Laplacian operator on the electric potential ($\nabla^2\phi$) as well as the charge density.

4.1. Seven-Probe Scheme

A seven-probe scheme, which is similar to the electric potential measurement of the MMS at high altitude orbits, is shown in Figure 8. All probes are placed on three axes of the Cartesian coordinate system. The spatial parameters are $x_2 = -x_1 = L_x$, $y_2 = -y_1 = L_y$, and $z_2 = -z_1 = L_z$. By taking differences, the linear and quadratic gradients at second-order accuracy can be obtained to estimate the charge density at the center.

The linear and quadratic gradients along the x-axis are

$$\begin{cases}\partial_x\phi = \dfrac{\phi_{x2} - \phi_{x1}}{2L_x} \\ \partial_x^2\phi = \dfrac{\dfrac{\phi_{x2}-\phi_0}{L_x} - \dfrac{\phi_0 - \phi_{x1}}{L_x}}{L_x} = \dfrac{(\phi_{x2}+\phi_{x1}) - 2\phi_0}{{L_x}^2}\end{cases} \tag{8}$$

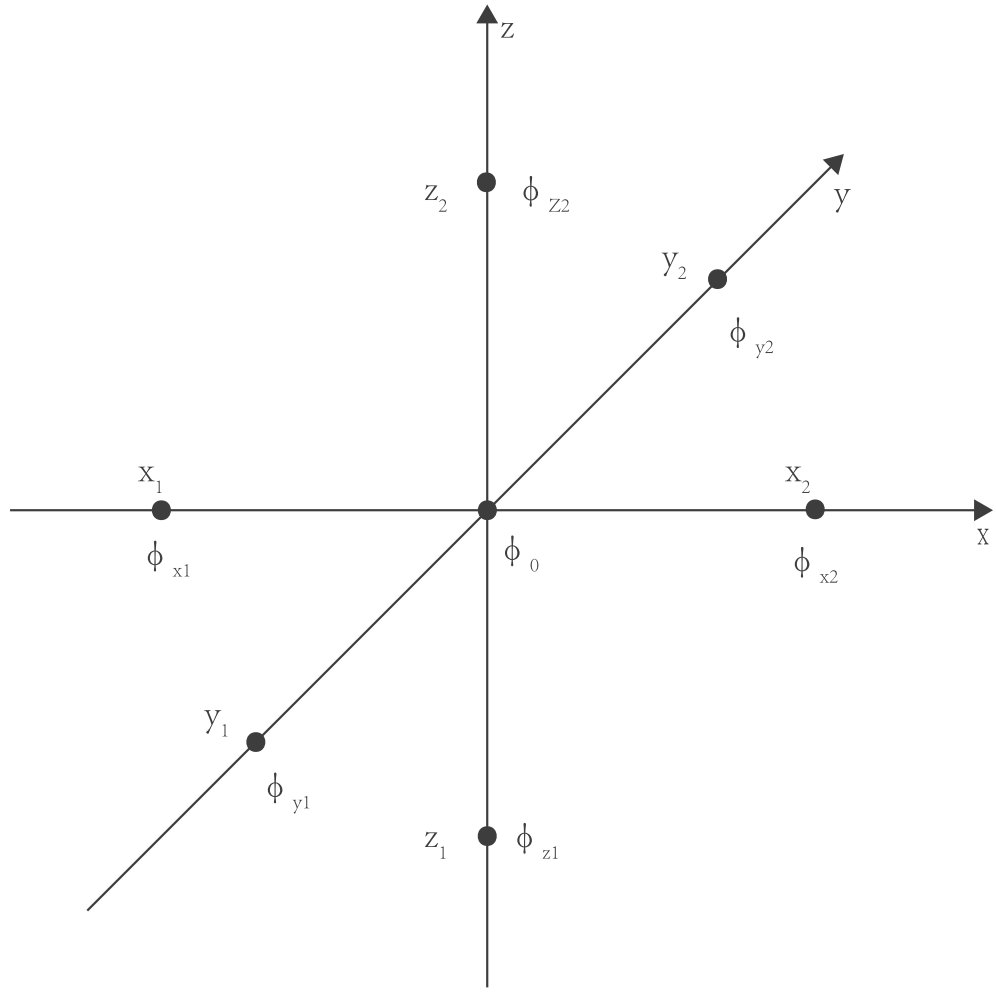

Figure 8. A schematic view of the seven-probe measurement of the charge density. The probes are indicated by black dots.

Similarly, the linear and quadratic gradients along the y-axis are

$$\begin{cases} \partial_y \phi = \dfrac{\phi_{y2} - \phi_{y1}}{2L_y} \\ \partial_y^2 \phi = \dfrac{(\phi_{y2} + \phi_{y1}) - 2\phi_0}{L_y^2} \end{cases} \tag{9}$$

The linear and quadratic gradients along the z-axis are

$$\begin{cases} \partial_z \phi = \dfrac{\phi_{z2} - \phi_{z1}}{2L_z} \\ \partial_z^2 \phi = \dfrac{(\phi_{z2} + \phi_{z1}) - 2\phi_0}{L_z^2} \end{cases} \tag{10}$$

The linear and quadratic gradients are both accurate to second order.

However, in actual measurements, the central probe is inside the spacecraft and cannot determine the electric potential accurately. To improve this measurement, the central probe is replaced by another two additional probes located on the z-axis. The algorithm for this is shown in the following section. It is noted the seven-probe scheme can be still applied to the electric field and charge density measurements in ground-based laboratory experiments.

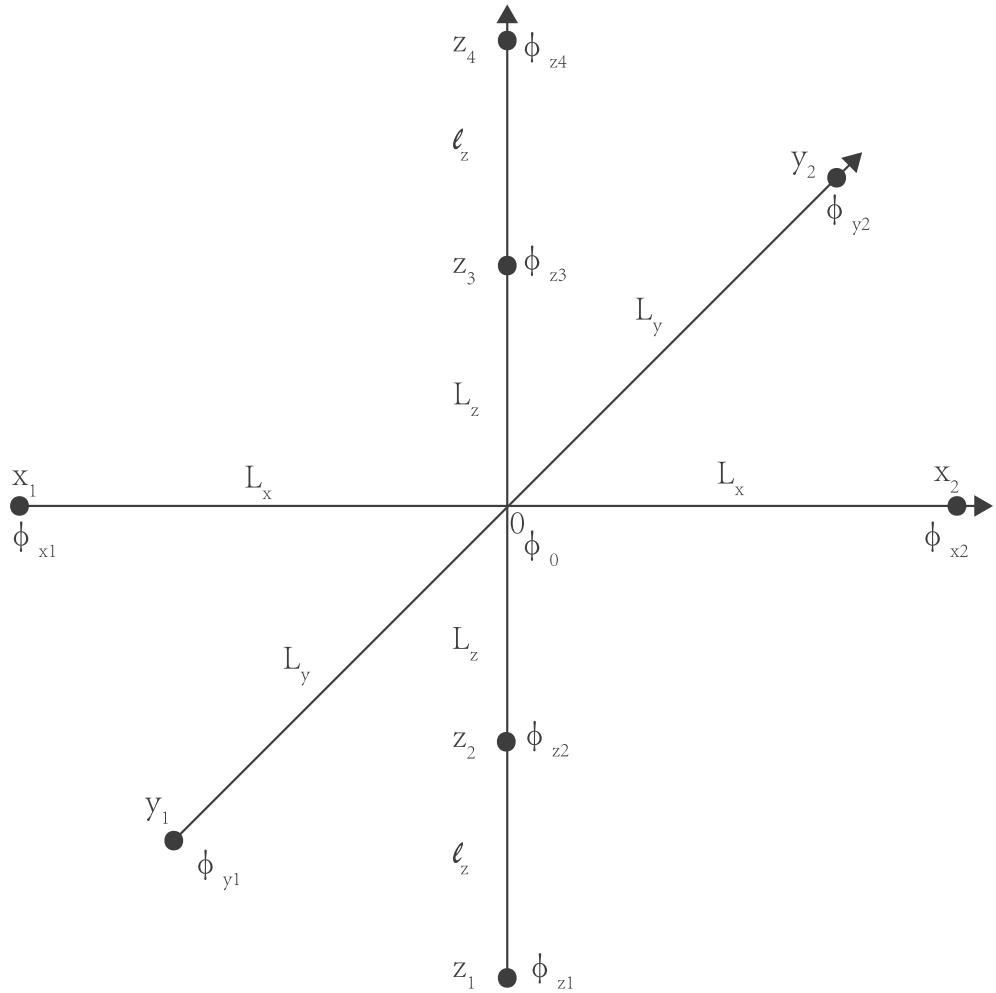

Figure 9. A schematic view of the eight-probe measurement of charge density.

4.2. Eight-Probe Scheme

The eight-probe scheme is shown in Figure 9 with $x_2 = -x_1 = L_x$, $y_2 = -y_1 = L_y$, $z_3 = -z_2 = L_z$, and $z_4 = -z_1 = L_z + l_z$. The algorithm is constructed as follows.

The four electric potentials observed by the probes on the z-axis can be expressed as a Taylor series. By keeping the first five terms we get

$$\left\{\phi_{z1} = \phi_0 + z_1\partial_z\phi + \frac{1}{2}{z_1}^2\partial_z{}^2\phi + \frac{1}{3!}{z_1}^3\partial_z{}^3\phi + \frac{1}{4!}{z_1}^4\partial_z{}^4\phi \right. \tag{11}$$

$$\left\{\phi_{z2} = \phi_0 + z_2\partial_z\phi + \frac{1}{2}{z_2}^2\partial_z{}^2\phi + \frac{1}{3!}{z_2}^3\partial_z{}^3\phi + \frac{1}{4!}{z_2}^4\partial_z{}^4\phi \right. \tag{12}$$

$$\left\{\phi_{z3} = \phi_0 + z_3\partial_z\phi + \frac{1}{2}{z_3}^2\partial_z{}^2\phi + \frac{1}{3!}{z_3}^3\partial_z{}^3\phi + \frac{1}{4!}{z_3}^4\partial_z{}^4\phi \right. \tag{13}$$

$$\left\{\phi_{z4} = \phi_0 + z_4\partial_z\phi + \frac{1}{2}{z_4}^2\partial_z{}^2\phi + \frac{1}{3!}{z_4}^3\partial_z{}^3\phi + \frac{1}{4!}{z_4}^4\partial_z{}^4\phi \right. \tag{14}$$

Summing up the above four equations leads to

$$(\phi_{z1} + \phi_{z2} + \phi_{z3} + \phi_{z4}) = 4\phi_0 + \frac{1}{2}(z_1^2 + z_2^2 + z_3^2 + z_4^2)\partial_z{}^2\phi + \frac{1}{4!}(z_1^4 + z_2^4 + z_3^4 + z_4^4)\partial_z{}^4\phi \tag{15}$$

The electric potential at the center is therefore

$$\phi_0 = \frac{1}{4}(\phi_{z1} + \phi_{z2} + \phi_{z3} + \phi_{z4}) - \frac{1}{8}(z_1^2 + z_2^2 + z_3^2 + z_4^2)\partial_z{}^2\phi - \frac{1}{96}(z_1^4 + z_2^4 + z_3^4 + z_4^4)\partial_z{}^4\phi \tag{16}$$

Subtracting Equation 11 from Equation 14 and Equation 12 from Equation 13 gives

$$\begin{cases} \phi_{z4} - \phi_{z1} = (z_4 - z_1)\partial_z\phi + \frac{1}{3!}({z_4}^3 - {z_1}^3)\partial_z{}^3\phi \\ \phi_{z3} - \phi_{z2} = (z_3 - z_2)\partial_z\phi + \frac{1}{3!}({z_3}^3 - {z_2}^3)\partial_z{}^3\phi \end{cases} \tag{17}$$

or

$$\begin{cases} \phi_{z4} - \phi_{z1} = 2z_4\partial_z\phi + \frac{1}{3}{z_4}^3\partial_z{}^3\phi \\ \phi_{z3} - \phi_{z2} = 2z_3\partial_z\phi + \frac{1}{3}{z_3}^3\partial_z{}^3\phi \end{cases} \tag{18}$$

Then, we get the linear gradient along the z-axis at the center as

$$\partial_z\phi = \frac{{z_3}^3(\phi_{z4} - \phi_{z1}) - {z_4}^3(\phi_{z3} - \phi_{z2})}{2z_4{z_3}^3 - 2z_3{z_4}^3} \tag{19}$$

The expression above is of fourth-order accuracy. On the other hand, from Equation 17, the third-order derivative of electric potential along the z-axis is

$$\partial_z{}^3\phi = \frac{3z_3(\phi_{z4} - \phi_{z1}) - 3z_4(\phi_{z3} - \phi_{z2})}{z_3{z_4}^3 - z_4{z_3}^3} \tag{20}$$

The expression above is of second-order accuracy.

Subtracting the sum of Equation 12 and Equation 13 from the sum of Equation 11 and Equation 14, we get

$$(\phi_{z4} + \phi_{z1}) - (\phi_{z3} + \phi_{z2}) = \frac{1}{2}({z_1}^2 + {z_4}^2 - {z_2}^2 - {z_3}^2)\partial_z{}^2\phi + \frac{1}{4!}({z_1}^4 + {z_4}^4 - {z_2}^4 - {z_3}^4)\partial_z{}^4\phi \tag{21}$$

The second-order derivative is, therefore,

$$\partial_z{}^2\phi = \frac{2(\phi_{z4} + \phi_{z1} - \phi_{z3} - \phi_{z2})}{({z_1}^2 + {z_4}^2 - {z_2}^2 - {z_3}^2)} - \frac{1}{12}\frac{({z_1}^4 + {z_4}^4 - {z_2}^4 - {z_3}^4)}{{z_1}^2 + {z_4}^2 - {z_2}^2 - {z_3}^2}\partial_z{}^4\phi \tag{22}$$

The expression above is of second-order accuracy.

Substituting Equation 22 into Equation 16, we get the corrected potential ϕ_0 at the center as

$$\phi_0 = \frac{1}{4}(\phi_{z1} + \phi_{z2} + \phi_{z3} + \phi_{z4}) - \frac{1}{4}\frac{z_1^2 + z_2^2}{{z_1}^2 - {z_2}^2}(\phi_{z4} + \phi_{z1} - \phi_{z3} - \phi_{z2}) + \frac{1}{24}z_1^2z_2^2\partial_z{}^4\phi \tag{23}$$

The above expression is of fourth-order accuracy because the expression is truncated at the fourth-order term.

Furthermore, by neglecting high order terms, we get the estimators for the potential and its linear and quadratic gradients at the center as

$$\begin{cases} \partial_z{}^2\phi = \frac{(\phi_{z4} + \phi_{z1}) - (\phi_{z3} + \phi_{z2})}{l_z(2L_z + l_z)} \end{cases} \tag{24}$$

$$\begin{cases} \partial_z\phi = \frac{(L_z + l_z)^3(\phi_{z3} - \phi_{z2}) - {L_z}^3(\phi_{z4} - \phi_{z1})}{2L_z(L_z + l_z)(2l_zL_z + {l_z}^2)} \end{cases} \tag{25}$$

$$\begin{cases} \phi_0 = \frac{1}{4}(\phi_{z1} + \phi_{z2} + \phi_{z3} + \phi_{z4}) - \frac{(L_z + l_z)^2 + L_z^2}{4l_z(2L_z + l_z)}(\phi_{z4} + \phi_{z1} - \phi_{z3} - \phi_{z2}) \end{cases} \tag{26}$$

As stated above, the second-order derivative along the z-axis is of second-order accuracy. The potential and its first-order derivative along the z-axis are of fourth-order accuracy.

Similar to the seven-probe scheme, the first-order and second-order derivatives of the potential along the x-axis and y-axis are subjected to Equations 8 and 9. The central potential ϕ_0 is calculated with Equation 26. The first-order and second-order derivatives along the x-axis and y-axis are of second-order accuracy.

The electric field at the center is

$$\mathbf{E} = -\hat{\mathbf{e}}_x \partial_x \phi - \hat{\mathbf{e}}_y \partial_y \phi - \hat{\mathbf{e}}_z \partial_z \phi \tag{27}$$

Using the Poisson Equation 4, the charge density is obtained as

$$\begin{aligned} \rho &= -\varepsilon_0(\partial_x{}^2\phi + \partial_y{}^2\phi + \partial_z{}^2\phi) \\ &= -\varepsilon_0 \left[\frac{(\phi_{x2} + \phi_{x1}) - 2\phi_0}{L_x^2} + \frac{(\phi_{y2} + \phi_{y1}) - 2\phi_0}{L_y^2} + \frac{(\phi_{z4} + \phi_{z1}) - (\phi_{z3} + \phi_{z2})}{l_z(2L_z + l_z)} \right] \end{aligned} \tag{28}$$

where ϕ_0 is given by Equation 26.

The eight-probe scheme will now be examined for the electric field produced by a uniformly charged ball.

The relationship between the relative truncation errors and the relative measurement scale, L/D, is studied when we set $L_x = L_y = L_z = l_z$ and scale up and down the distances between the spacecraft to adjust L/D. Due to the broken spherical symmetry, two points inside the ball, [0.5, 0, 0] and [0.5, 0.4, 0.3], and two points outside of the ball, [8, 0, 0] and [2, 2, 6], are chosen as the representative points. The modeled results are shown in Figure 10. The quadratic gradient in the ball is close to a constant and the charge density here is a constant. The truncation errors given by the algorithm, as shown in Figures 10a and 10b, are negligible in this case. The charge density outside the ball is zero, and the calculated density, amounting to 10^{-4} as shown by the dashed lines in Figures 10c and 10d, is fairly close to zero. Note that the scale is one in the modeled system. As $L/D < 0.1$, the truncation errors of the quadratic gradient are less than 2%. It can be seen that the relative errors of the quadratic gradient and hence the charge density are at second order in *L/D*.

For real measurements in space, the distances between the probes along the z-axis, L_z and l_z, are much smaller than those along the other axes, L_x and L_y. The truncation error in real case, therefore, should be less than evaluated when setting them all equal.

An error analysis on the eight-probe scheme using the charged ball model of $\rho = b/r^2$ is also conducted. The result as shown in Figure S5 have further confirmed the accuracy of this algorithm. This eight probe scheme is potentially applied for the net charge measurements on the high altitude orbits, for which the spacecraft is spinning thus that the four probes can stretch out at the ends of the four wire booms on the spin plane as shown in Figure 9. Performing similar error analysis as in Section 3, it is found the sensitivity of the probes is required to reach 0.5 mV, which still needs technical efforts to achieve in the future.

5. Summary and Discussions

Preliminary explorations for measuring the net charge density in space have been presented in this study. Three schemes for the charge density measurements have been developed.

The first scheme deduces the charge density based on four spacecraft electric field measurements. Based on the electric fields ($\boldsymbol{E}_\alpha$, $\alpha = 1, 2, 3, 4$) observed at the four spacecraft, we can obtain the gradient of the electric field at the barycenter of the constellation, $(\nabla \boldsymbol{E})_c$, and furthermore, the divergence of the electric field, $(\nabla \cdot \boldsymbol{E})_c$. The Gaussian theorem yields the charge density as $\rho = \epsilon \nabla \cdot \boldsymbol{E}$. This algorithm requires the constellation not to be

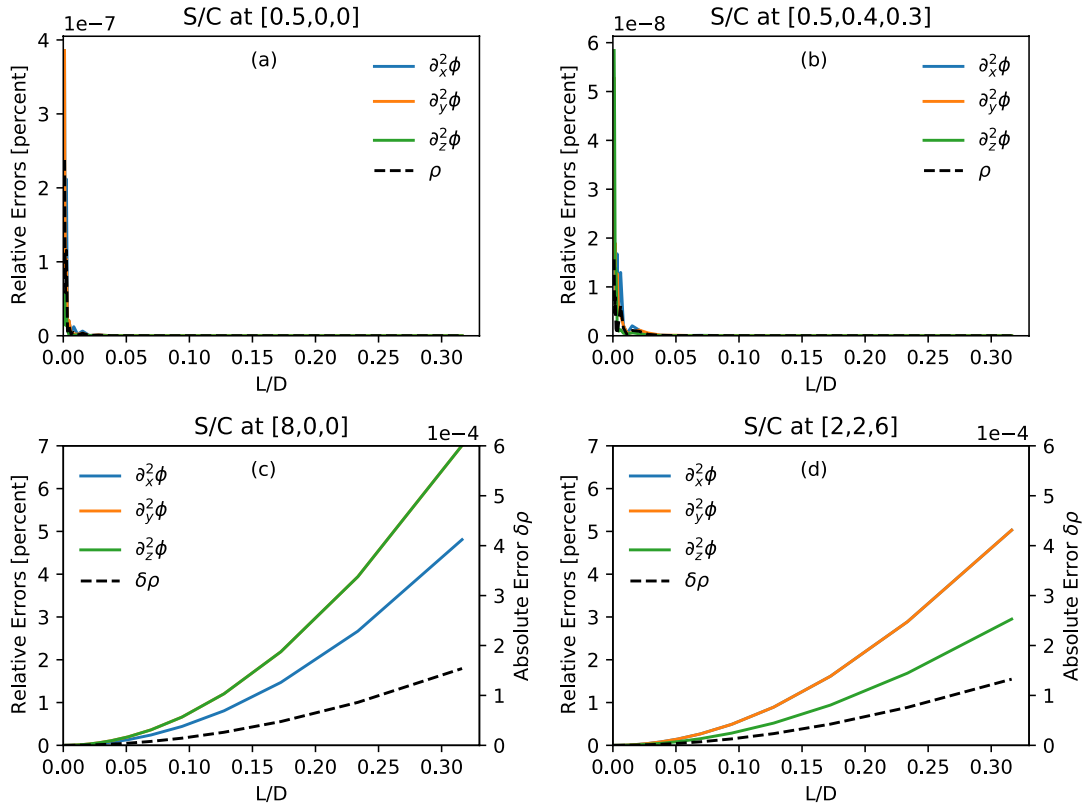

Figure 10. The dependence of the truncation errors of the calculations by using the eight-probe scheme on the relative measurement scale L/D for the case of a uniformly charged ball. Panels (a) and (b) show the relative truncation errors of the quadratic gradient of the electric potential (solid lines) and the charge density (dashed lines) at [0.5, 0, 0] and [0.5, 0.4, 0.3] in the ball, respectively. Panels (c) and (d) show the relative truncation errors of the quadratic gradient of the electric potential (solid lines and left vertical axis) and the absolute errors of the charge density (dashed lines and right vertical axis) at [8, 0, 0] and [2, 2, 6] out of the ball. In panel (c), the orange line orange line is overlayed with the green line. In panel (d), the blue line is overlayed with the orange line.

distributed in a plane or linearly. In other words, the three eigenvalues of the volumetric tensor of the constellation should be non-vanishing. Based on this algorithm, an analysis on the electric field data acquired during a dayside magnetopause crossing event by the MMS constellation shows a charge separation in the magnetopause boundary layer and that the positive charges are accumulated on the magnetospheric side while the negative charges are accumulated on the magnetosheath side. A normal electric field pointing at the magnetosheath is also discovered. This confirms a previous theoretical prediction (Hughes, 1995; Parks, 1991).

Another charge density measurement scheme is based on 10 or more electric potential probes. By using a newly developed algorithm (C. Shen et al., 2021), the linear gradient, $(\nabla\phi)_c$, and the quadratic gradient, $(\nabla\nabla\phi)_c$, of the electric potential at the center of the probes can be calculated from the $N \geq 10$ electric potentials, $\phi_\alpha(\alpha = 1, 2, \cdots, N)$, as measured at the N probes. Furthermore, the electric field and the net charge density at the center of the probes can be calculated using $\mathbf{E} = -(\nabla\phi)_c$ and the Poisson equation, $\rho = -\epsilon\nabla^2\phi$, respectively.

This scheme requires the probes to be distributed uniformly. In other words, the eigenvalues of the 6×6 matrix $\mathfrak{R}$ should be non-vanishing (C. Shen et al., 2021). The accuracy of the charge density estimated by the algorithm is of first order and that of the electric field is of second order. Modeling also shows that more probes lead to higher accuracy.

Finally, two other schemes are presented to measure the electric charge density, which improve on the existing schemes for electric field observations onboard spacecraft. If one more electric potential probe is added in addition to the six electric potential probes of the electric field equipment onboard the MMS spacecraft (that are distributed symmetrically on the three axes of the Cartesian coordinate system), the charge density can be derived

along with the electric field vectors. The seventh probe is placed at the origin of the coordinate system. Due to the shielding potential of the spacecraft, this seven-probe scheme cannot be applied to measurements in space. However, it can be utilized in charge density measurements in ground-based laboratory experiments. Alternatively, by placing two more probes symmetrically on the two stiff booms in the six-point scheme of the MMS constellation, the eight-probe scheme will work for charge density measurements in space. The simulation test shows that the estimated electric field is of fourth-order accuracy and the charge density is of second-order accuracy. The truncation errors contained in this scheme are much less than those in the 10-probe scheme. The implementation of this scheme requires further development in the future.

Conflict of Interest

The authors declare no conflicts of interest relevant to this study.

Data Availability Statement

The MMS data were obtained from the MMS Science Data Center (http://lasp.colorado.edu/mms/sdc/). The authors thank the MMS plasmas and field terms for providing these high-quality data.

Acknowledgments
This study was supported by the National Natural Science Foundation (NSFC) of China (Grant no. 41874190 and 42130202) and the Shenzhen Technology Project (JCYJ20190806144013077).

References

Akasofu, S.-I. (1981). The aurora: An electrical discharge phenomenon surrounding the Earth. *Reports on Progress in Physics*, *44*, 1123–1149. https://doi.org/10.1088/0034-4885/44/10/003

Alfvén, H., & Falthammar, C.-G. (1963). *Cosmical electrodynamics: Fundamental principles* (2nd ed., p. 201). Clarendon Press.

Argall, M., Shuster, J., Dors, I., Genestreti, K., Nakamura, T., Torbert, R., et al. (2019). How neutral is quasi-neutral: Charge density in the reconnection diffusion region observed by MMS. *Earth and Space Science Open Archive*. https://doi.org/10.1002/essoar.10501410.1

Axford, W. I. (1968). The polar wind and the terrestrial helium budget. *Journal of Geophysical Research*, *73*, 6855–6859. https://doi.org/10.1029/ja073i021p06855

Berthelier, J. J., Godefroy, M., Leblanc, F., Malingre, M., Menvielle, M., Lagoutte, D., et al. (2005). ICE, the electric field experiment on DEMETER. *Planetary and Space Science*, *54*(5), 456–471. https://doi.org/10.1016/j.pss.2005.10.016

Bittencourt, J. A. (2004). *Fundamentals of plasma physics* (p. 256). Springer.

Block, L. (1975). Double layers. In B. Hultqvist, & L. Stenflo (Eds.), *Physics of the hot plasma in the magnetosphere* (pp. 229–249). Springer. https://doi.org/10.1007/978-1-4613-4437-7_11

Burch, J. L., Moore, T. E., Torbert, R. B., & Giles, B. L. (2016). Magnetospheric Multiscale overview and science objectives. *Space Science Reviews*, *199*(1–4), 5–21. https://doi.org/10.1007/978-94-024-0861-4_2

Chanteur, G. (1998). Spatial interpolation for four spacecraft: Theory. In G. Paschmann, & P. W. Daly (Eds.), *Analysis methods for multi-spacecraft data* (p. 349). ESA Publications Division.

Ergun, R. E., Tucker, S., Westfall, J., Goodrich, K. A., Malaspina, D. M., Summers, D., et al. (2016). The axial double probe and fields signal processing for the MMS mission. *Space Science Reviews*, *199*, 167–188. https://doi.org/10.1007/s11214-014-0115-x

Escoubet, C. P., Fehringer, M., & Goldstein, M. (2001). Introduction: The Cluster mission. *Annales Geophysicae*, *19*, 1197–1200. https://doi.org/10.5194/angeo-19-1197-2001

Haaland, S., Hasegawa, H., Paschmann, G., Sonnerup, B., & Dunlop, M. (2021). 20 years of Cluster observations: The magnetopause. *Journal of Geophysical Research: Space Physics*, *126*, e2021JA029362. https://doi.org/10.1029/2021ja029362

Harris, E. G. (1962). On a plasma sheath separating regions of oppositely directed magnetic field. *Nuovo Cimento*, *23*, 115–121. https://doi.org/10.1007/BF02733547

Harvey, C. C. (1998). Spatial gradients and the volumetric tensor. In G. Paschmann, & P. W. Daly (Eds.), *Analysis methods for multi-spacecraft data* (p. 307). ESA Publications Division.

Hasegawa, A., & Sato, I. (1989). Space plasma physics. In *Stationary processes* (Vol. 1, pp. 153–156). Springer-Verlag.

Hughes, W. T. (1995). The magnetopause, magnetotail, and magnetic reconnection. In M. Kivelson, & C. T. Russell (Eds.), *Introduction to space physics* (Ch. 9, p. 230). Cambridge University Press. https://doi.org/10.1017/9781139878296.010

Lee, L. C., & Kan, J. R. (1979). A unified kinetic model of the tangential magnetopause structure. *Journal of Geophysical Research Space Physics*, *84*(A11), 6417–6426. https://doi.org/10.1029/ja084ia11p06417

Lemaire, J., & Pierrard, V. (2001). Kinetic models of solar and polar winds. *Astrophysics and Space Science*, *277*, 169–180. https://doi.org/10.1007/978-94-010-0904-1_22

Lindqvist, P. A., Olsson, G., Torbert, R. B., King, B., Granoff, M., Rau, D., et al. (2016). The spin-plane double probe electric field instrument for MMS. *Space Science Reviews*, *199*, 137–165. https://doi.org/10.1007/s11214-014-0116-9

Michael, C. K. (2014). *The Earth's electric field: Sources from Sun to Mud*. Elsevier.

Mozer, F. S. (1973). Analyses of techniques for measuring dc and ac electric fields in the magnetosphere. *Space Science Reviews*, *14*, 272–313. https://doi.org/10.1007/bf02432099

Mozer, F. S., & Bruston, P. (1967). Motion of artificial ion clouds in upper atmosphere. *Journal of Geophysical Research*, *72*, 1109–1114. https://doi.org/10.1029/jz072i003p01109

Parks, G. K. (1991). *Physics of space plasmas: An introduction* (pp. 355–369). Addison-Wesley Publishing Co.

Paschmann, G., Haaland, S., Sonnerup, B. U. O., Hasegawa, H., Georgescu, E., Klecker, B., et al. (2005). Characteristics of the near-tail dawn magnetopause and boundary layer. *Annales de Geophysique*, *23*(4), 1481–1497. https://doi.org/10.5194/angeo-23-1481-2005

Paschmann, G., Melzner, F., Frenzel, R., Vaith, H., Parigger, P., Pagel, U., et al. (1997). The electron drift instrument for Cluster. *Space Science Reviews*, *79*, 233–269. https://doi.org/10.1007/978-94-011-5666-0_10

Pedersen, A. F., Mozer, F. S., & Gustafsson, G. (1998). Electric field measurements in a tenuous plasma with spherical double probes. In R. F. Pfaff, J. E. Borovsky, & D. T. Young (Eds.), *Measurement techniques in space plasmas—Fields* (pp. 1–12). AGU Geophysical Monograph. https://doi.org/10.1029/gm103p0001

Pollock, C., Moore, T. E., Jacques, A., Burch, J., Gliese, U., Saito, Y., et al. (2016). Fast plasma investigation for magnetospheric multiscale. *Space Science Reviews*, *199*(1–4), 331–406. https://doi.org/10.1007/s11214-016-0245-4

Raadu, M. A. (1989). The physics of double layers and their role in astrophysics. *Physics Reports*, *178*, 25–97. https://doi.org/10.1016/0370-1573(89)90109-9

Robert, P., Roux, A., Harvey, C. C., Dunlop, M. W., Daly, P. W., & Glassmeier, K. H. (1998). Tetrahedron geometric factors. In G. Paschmann, & P. W. Daly (Eds.), *Analysis methods for multi-spacecraft data* (p. 323). ESA Publications Division.

Shen, C., Dunlop, M., Li, X., Liu, Z. X., Balogh, A., Zhang, T. L., et al. (2007). New approach for determining the normal of the bow shock based on Cluster four-point magnetic field measurements. *Journal of Geophysical Research*, *112*, A03201. https://doi.org/10.1029/2006JA011699

Shen, C., Li, X., Dunlop, M., Liu, Z. X., Balogh, A., Baker, D. N., et al. (2003). Analyses on the geometrical structure of magnetic field in the current sheet based on cluster measurements. *Journal of Geophysical Research*, *108*(A5), 1168. https://doi.org/10.1029/2002JA009612

Shen, C., Zhou, Y. F., Ma, Y. H., Wang, X. G., Pu, Z. Y., & Dunlop, M. (2021). A general algorithm for the linear and quadratic gradients of physical quantities based on 10 or more point measurements. *Journal of Geophysical Research: Space Physics*, *126*, e2021JA029121. https://doi.org/10.1029/2021ja029121

Shen, X. H., Zhang, X. M., Yuan, S. G., Wang, L. W., Cao, J. B., Huang, J. P., et al. (2018). The state-of-the-art of the China Seismo-Electromagnetic Satellite mission. *Science China Technological Sciences*, *8*(615), 634–642. https://doi.org/10.1007/s11431-018-9242-0

Tong, Y., Vasko, I., Mozer, F. S., Bale, S. D., Roth, I., Artemyev, A. V., et al. (2018). Simultaneous multispacecraft probing of electron phase space holes. *Geophysical Research Letters*, *45*(21), 11511–11519. https://doi.org/10.1029/2018GL079044

Torbert, R. B., Russell, C. T., Magnes, W., Ergun, R. E., Lindqvist, P.-A., LeContel, O., et al. (2016). The FIELDS Instrument Suite on MMS: Scientific objectives, measurements, and data products. *Space Science Reviews*, *199*, 105–135. https://doi.org/10.1007/s11214-014-0109-8

Treumann, R. A., & Baumjohann, W. (1997). *Advanced space plasma physics* (pp. 31155–33167). Imperial College Press.

Yau, A. W., Takumi, A., & Peterson, W. K. (2007). The polar wind: Recent observations. *Journal of Atmospheric and Solar-Terrestrial Physics*, *69*, 1936–1983. https://doi.org/10.1016/j.jastp.2007.08.010